JOURNAL OF GEOPHYSICAL RESEARCH, VOL. 106, NO. D14, PAGES 15,113–15,122, JULY 27, 2001

Large-eddy simulations of entrainment of cloud condensation nuclei into the Arctic boundary layer: May 18, 1998, FIRE/SHEBA case study

Hongli Jiang,[1] Graham Feingold,[2] William R. Cotton,[1] and Peter G. Duynkerke[3]

Abstract. Two sets of three-dimensional simulations of a springtime Arctic boundary layer cloud observed during the FIRE/SHEBA 1998 spring IOP were conducted to study the influence of entrainment of cloud condensation nuclei (CCN) at cloud top on cloud microphysical and dynamical structure, radiative properties, and cloud evolution. The model is a large-eddy version of the Regional Atmospheric Modeling System (RAMS) with explicit representation of the CCN spectrum and cloud droplet spectrum. The initial CCN concentration is a constant value of 30 cm^{-3} in the control run, while it varies from 30 cm^{-3} below cloud base to a peak of 250 cm^{-3} at the inversion in the sensitivity run. Results from the sensitivity run show that droplet concentrations increase about twofold, effective radii decrease by 9–15% from cloud top to cloud base, liquid water content increases about 21%, and no drizzle reaches the ground in comparison with results from the control run. The dynamic response becomes significant by the end of the 5 hour simulation, as reflected in more vigorous eddies in the sensitivity run. The response of the cloud optical properties to entrainment occurs from the beginning of the simulations. Cloud albedo increases 12%, while cloud optical depth increases 33%. These results are consistent with both observations and modeling studies. It is stressed that knowledge of boundary layer deepening is critical to prediction of cloud optical properties, both from the thermodynamical perspective, because the properties of the entrained air affect bulk cloud features such as liquid water path, and from the microphysical perspective because aerosol gradients across the top of the boundary layer can alter microphysical properties and, in turn, cloud optical properties.

1. Introduction

A large number of cumulus cloud studies [e.g., *Baker et al*., 1980; *Telford and Chai*, 1980] and stratiform cloud studies [e.g., *Telford and Wagner*, 1981; *Considine and Curry*, 1998] have shown that cloud microphysical properties are influenced by entrainment and mixing. Most of these studies have focused on the turbulent mixing of dry, warm, and presumably cleaner air from above with the cloudy air and its impact on the droplet spectra, without considering the cloud condensation nucleus (CCN) properties of the entrained air. Using a one-dimensional explicit mixing parcel model, *Su et al*. [1998] included CCN in the entrained air and found drop spectral broadening resulting from entrained CCN growing into small droplets.

Entrainment of cleaner free tropospheric air has been observed to result in a decrease in CCN concentration in tropospheric clouds [e.g., *Clarke et al*., 1996]. Cases with polluted air above the inversion are not uncommon [e.g., *Clarke*, 1993; *Clarke et al*., 1997; *Raes*, 1995], and the entrainment of such air, together with associated condensation nuclei (CN), could influence the number of CCN that activate at a given supersaturation.

Variations in CCN have the potential to alter cloud microphysical and optical properties through modifying the cloud particle phase, size, and concentration [e.g., *Twomey*, 1991; *Curry et al*., 1993]. The response of the cloud microphysical, radiative, and dynamical structure to a variation in CCN concentration has been investigated numerically in warm-season Arctic stratus [e.g., *Olsson et al*., 1998] and marine stratocumulus clouds [e.g., *Feingold et al*., 1994]. These studies support observational studies that show that an increase in CCN concentration produces a more reflective cloud composed of a larger number of smaller droplets for a given amount of liquid water.

Pollution of North American and Eurasian continental origin is believed to be one of the sources of arctic aerosols during the winter months. *Barrie* [1986] showed that particulate pollution in spring was found throughout the depth of the arctic air mass but was highest in the lowest 2 km. During the SHEBA/FIRE spring IOP (May 18, 1998) a high concentration of cloud nuclei in the air above the cloud was observed to overlie a fairly clean boundary layer. This situation is also fairly common in Californian boundary layers where polluted continental air sometimes overlies cleaner marine boundary layer air. In a numerical study, *Duda et al*. [1996] simulated such a case and showed that when air containing a sixfold higher concentration of CCN above cloud is entrained into cloud, a 6–9% increase in cloud albedo is simulated.

Because of the strong stability of the arctic boundary layer,

[1]Department of Atmospheric Science, Colorado State University, Fort Collins.
[2]NOAA, Environmental Technology Laboratory, Boulder, Colorado.
[3]Institute for Marine and Atmospheric Research Utrecht (IMAU), Utrecht University, Utrecht, Netherlands.

Paper number 2000JD900303.
0148-0227/01/2000JD900303$09.00

it has been hypothesized that the importance of cloud entrainment effects are only secondary, whereas the background air chemistry and CCN characteristics are the principal determinant of the drop size distribution [*Curry*, 1995].

To understand how the microphysical and dynamical structure and radiation properties of arctic stratus are modified by the entrainment of "polluted" air at cloud top in the arctic environment, we have performed a number of numerical simulations in a three-dimensional/LES framework with liquid-phase, bin-resolving microphysics [*Feingold et al*., 1996a]. The key issue to be addressed is how long it takes for differences in cloud dynamics and microphysics to develop in response to variations in CCN concentrations due to entrainment, and how this process affects the Arctic cloud evolution. Numerical simulations of the FIRE/SHEBA May 18 case are used to address this question. Where possible, comparison between the simulations are made with observational data; however, the case study is used more as a guidance for studying the contamination of the cloud by polluted air overriding the boundary layer than as a rigorous intercomparison with observations.

The paper is organized as follows: Section 2 contains a brief summary of the LES version of RAMS and the explicit microphysics model. Section 3 describes the chosen case and experiment design. Section 4 presents results from two three-dimensional runs: one using the CCN sounding observed on 18 May 1998 during the FIRE/SHEBA spring IOP, and the other using a vertically uniform CCN as a sensitivity test. Section 5 discusses and summarizes the results.

2. Model Description

The Regional Atmospheric Modeling System (RAMS) is a multipurpose modeling system that has been used to simulate drizzle production in marine stratocumulus [*Feingold et al*., 1996a; *Stevens et al*., 1998] and arctic boundary layer stratus [*Olsson et al*., 1998; *Harrington et al*., 1999]. In this investigation, RAMS is set up as a nonhydrostatic LES model combined with an explicit microphysics model [*Feingold et al*., 1994]. The predicted variables include the three velocity components (u, v, w), the Exner function (π), the ice-liquid water potential temperature (θ_{il}) [*Tripoli and Cotton*, 1981], and total water mixing ratio r_t on a vertically stretched Arakawa C-grid.

2.1. Explicit Microphysics Model

The explicit bin-resolving microphysics model is an accurate moment-conserving scheme, described in detail by *Tzivion et al*. 1987, 1989] and *Stevens et al*. [1996]. A brief description of the explicit microphysics model is given below. In this scheme, both the mass and the number mixing ratios are predicted for each bin. A total of 25 bins cover a drop spectrum ranging from 1.56 to 504 μm (radius), with mass doubling from one bin to the next. Predictive equations for both the mass and the number mixing ratios in each bin require an additional 50 scalars for the liquid cloud-related processes: condensation/evaporation, collision-coalescence, droplet activation from CCN, and sedimentation.

In some of our prior studies [*Stevens et al*., 1996] a rather simple-drop activation scheme was implemented whereby CCN were assumed to have a constant (in time and space) size distribution, and activation was calculated such that the number of cloud drops was based on the model-derived supersaturation but could not exceed the number concentration of CCN. Thus at each time step the drop concentration N_d was incremented by an amount

$$\Delta N_d = \max\left[0,\, N_{\mathrm{ccn}} \int_{r_{\mathrm{cut}}}^{\infty} f(r;\, r_g,\, \sigma_g)dr - \sum_{k=1}^{25} N_k\right], \quad (1)$$

where N_{ccn} is the total CCN concentration, r_{cut} is the smallest radius of CCN activated at the ambient supersaturation S, r_g is the median radius of CCN, σ_g is the geometric standard deviation of the CCN radii, and N_k is the number concentration of drops in size bin k. To explore aerosol-cloud interactions, one would ideally like to model the size-resolved aerosol spectrum [e.g., *Feingold et al*., 1996b] as well as the drop size distribution response to the aerosol spectrum. Because of the large computational expense of these simulations we opted for a more simplified droplet activation scheme based on (1). We assume that the CCN size distribution is constant throughout the model domain (i.e., r_g and σ_g are constant) and that only N_{ccn} varies as one passes from the clean boundary layer to the rather polluted air aloft. The representation of the aerosol is reduced to prognosing N_{ccn}, rather than a set of parameters that describe the full distribution of CCN particles. Since larger particles are activated more readily, they would tend to exist in lower concentrations than represented by $f(r;\, r_g,\, \sigma_g)$; therefore the assumption that $f(r;\, r_g,\, \sigma_g)$ is constant implies an overestimate in activation rates. This overestimate is controlled, to some extent, by the fact that enhanced activation will suppress subsequent activation by providing a stronger sink for vapor and lowering the supersaturation. For the goals of our study we feel that this representation is sufficient, although we recognize that variations in both the size distribution and the chemical composition of the particles may have significant impact under certain circumstances [*Feingold et al*., 1999]. Note that outside of cloud the prognosed field N_{ccn} is the number concentration of CCN in cubic centimeters, whereas within the cloud, it represents the potential number of drops that can be activated and not the number concentration of unscavenged CCN. The latter can easily be calculated as

$$N_{\mathrm{unscavenged}} = N_{\mathrm{ccn}} - N_d. \quad (2)$$

Unlike *Feingold et al*. [1996b], CCN particles are not tracked within drops and the current simplified treatment has an inherent assumption that the CCN concentration would be unmodified (in both number and size) on complete evaporation of drops. For clouds with very weak collision-coalescence, such as the cases examined here, this is quite reasonable.

2.2. Two-Stream Radiation Model

A two-stream radiative transfer model is utilized for this study [*Harrington et al*., 1999]. The two-stream model solves the radiative transfer equations for three gaseous constituents, H_2O, O_3, and CO_2 and the optical effects of the hydrometeor size spectra. Gaseous absorption is calculated by following the fast exponential sum-fitting of transmissions method proposed by *Ritter and Geleyn* [1992]. Lorenz-Mie theory is used to compute the optical properties for water drops, while the theory of *Mitchell et al*. [1996] is used for nonspherical ice crystals. The radiative transfer model responds to the bin microphysical model using a method whereby the optical properties based on bin averages of the appropriate quantities are computed beforehand and then summed with appropriate weights during the simulation [*Harrington et al*., 2000].

3. Experiment Design

3.1. Case Description and Model Initiation

The case chosen for this study was a boundary layer cloud observed on May 18, 1998, in the FIRE/SHEBA field experiment. The boundary layer cloud was mostly liquid in the layer 200–500 m, with an inversion height near 500 m. Winds were light easterly at the surface. On that particular day the CCN sounding exhibited concentrations ranging from 30 cm^{-3} below cloud base to a peak of 250 cm^{-3} at the inversion, lowering to 160 cm^{-3} at 700 m.

Two sets of simulations are conducted to investigate the entrainment of CCN from above the boundary layer into the cloudy layer and how the entrained air affects microphysical and radiative properties of the boundary layer. The model is initialized with the sounding taken during Research Flight 5, onboard the SHEBA C-130 aircraft. In the control run, the initial CCN concentration is set to 30 cm^{-3}, a value close to that observed in the subcloud layer, throughout the domain (hereinafter referred to as N30). In the sensitivity run, the initial CCN concentration is derived from the CCN data collected during FIRE III using an instantaneous CCN spectrometer [*Hudson*, 1989] activated at 0.8% supersaturation (hereinafter referred to as N250). A 5 hour long simulation is performed for both cases. For comparison purposes, both the initial CCN profile used for N250 and the observed CCN profile, active at 0.8% supersaturation, are shown in Figure 1. Note that the CCN concentration used in the N250 run has a constant value of 30 cm^{-3} up to 400 m from the surface, with a 220 cm^{-3} jump crossing the initial cloud top.

The initial total water mixing ratio r_t, dry potential temperature θ, horizontal wind u, v, and liquid water content (LWC) are given in Figure 2.

3.2. Model Configuration and Boundary Condition

Simulations are done in a three-dimensional (3-D) framework. The 3-D simulation has a domain of $45 \times 45 \times 55$ grid points with a 50 m grid spacing in the horizontal and 25 m grid spacing in the vertical from the surface to the domain top (1375 m). The time step is 2 s.

The lateral boundary conditions are cyclic. The boundary condition at the model top corresponds to a rigid lid, with a Rayleigh friction absorbing layer applied to the momentum equations and to the thermodynamic equation. The surface parameterization based on that of *Louis* [1979] is used, and the bottom boundary is specified to be consistent with surface conditions observed during FIRE/SHEBA, with a specified surface temperature of 266 K. The large-scale subsidence is prescribed by $w_{sub} = -Dz$. Where $D = 5. \times 10^{-6}$ s^{-1} is the large-scale divergence, and z is the model height in meters. This gives an averaged subsidence velocity at the inversion of -0.25 cm s^{-1}.

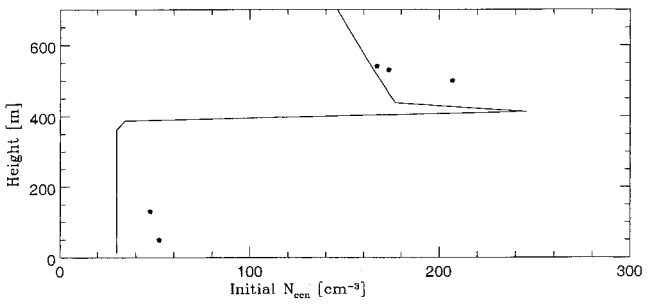

Figure 1. Vertical profile of the CCN concentration for the N250 run (solid line) and the observed CCN profile activated at 0.8% supersaturation (dots).

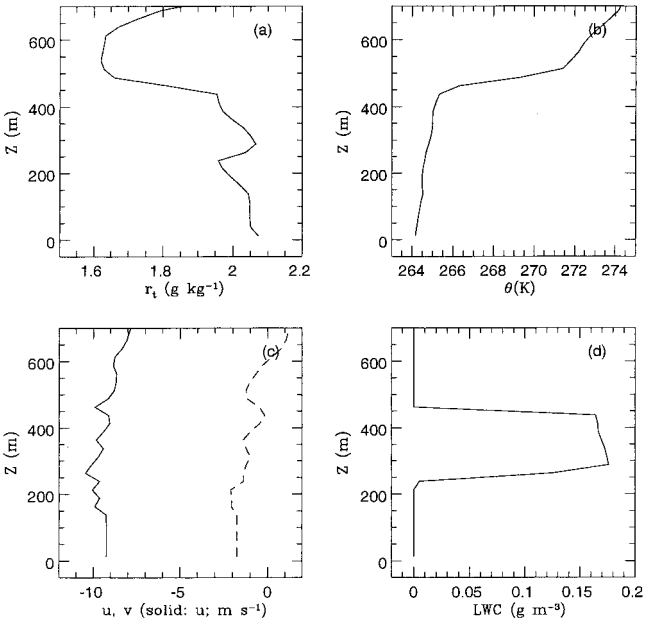

Figure 2. Vertical profiles of the initial conditions: (a) total water mixing ratio, (b) dry potential temperature, (c) horizontal wind components (u, solid line; v, dashed line), and (d) liquid water content (LWC).

4. Simulation Results

Selected time series and mean profiles of different cloud properties averaged over the horizontal ($x - y$) plane (referred to as layer averages) and then time averaged over the last hour (5 hours) will be shown. Comparison between the two runs will be presented and compared with the available observational data. In general, the model requires about 2 hours to produce the initial cloud and establish the resolved-scale turbulence. Thus we will only look at various fields after the spin-up period.

Figure 3 shows selected time sequences from both runs. The local height of the inversion is determined by linearly interpolating grid values of total water mixing ratio r_t to 1.8 g kg^{-1}, which gives the corresponding interpolated inversion height in a column. Note that 1.8 g kg^{-1} is the averaged observed value in the inversion. The inversion height z_i (Figure 3a) is then defined as the horizontal average of these inversion height values; this is in general not a model level. The average rate of change of z_i is calculated later to give the time resolution of the entrainment velocity w_e ($=dz_i/dt - w_{sub}$) and averaged over the last 3 hours of simulation for comparison with the estimate from observations. Value z_i shows a steady increase with time for both runs except that z_i is higher in the N250 run, suggesting stronger mixing at the inversion. Liquid water path, LWP (Figure 3b) is very similar for much of the simulation in both runs except for the last hour when LWP is about 10% higher in the N250 run. The reduction in LWP for N30 is associated with the increase in the surface drizzle flux (Figure 3c). The column maximum value of $(w'w')^{1/2}$, labeled σ_w in Figure 3d, does not show strong correlation with either the LWP or the surface

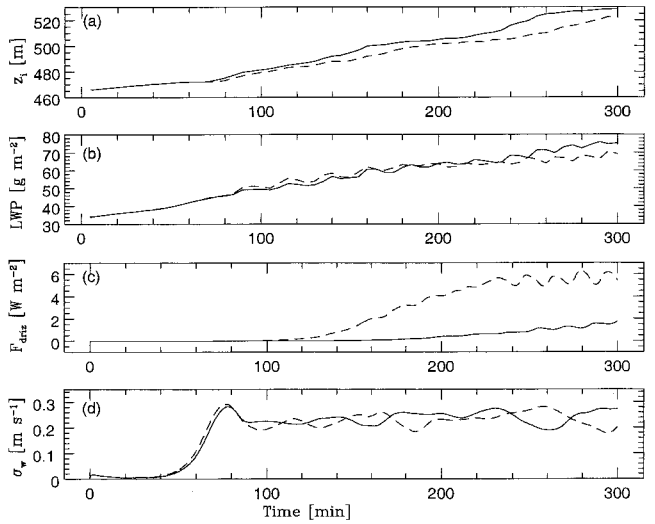

Figure 3. Temporal evolution of (a) inversion height, (b) LWP, (c) surface drizzle flux (W m^{-2}), (d) maximum value of $\langle (w'w') \rangle^{1/2}$ for both runs. The solid line denotes the N250 run, and the dashed line denotes the N30 run.

drizzle flux. During the last 40 min of the N30 simulation, however, the decrease in σ_w may correspond to the depletion in LWP resulting from drizzle and the feedback to dynamics incurred by drizzle [*Stevens et al.*, 1998]. Note that this reduction in LWP and σ_w occurs despite the fact that the drizzle flux is approximately constant (Figure 3c), so that the response appears to be due to the integrated amount of drizzle rather than the increase in the drizzle rate [see also *Feingold et al.*, 1999].

It is known that the CCN concentration determines cloud droplet number concentration N_d. The dependence of cloud optical depth τ and cloud albedo A on N_d has long been established for nonprecipitating clouds [e.g., *Platnick and Twomey*, 1994] and for drizzling clouds [e.g., *Feingold et al.*, 1997]. In this study, the change in CCN concentration is mainly from above-cloud air parcels containing higher concentrations of CCN entrained into the cloud layer and through mixing at the cloud top. Figure 4 shows the layer averages of CCN concentration (N_{ccn}, potential drop number that can be activated in the cloud layer), drop concentration (N_d), and unscavenged CCN concentration ($N_{unscavenged}$) at different simulation times for the N250 run (see (2) in the model section for a detailed explanation). N_{ccn} is quickly doubled from the initial value in the cloud layer, while it stays low below cloud at 2 hours (solid line). It is interesting to note that the maximum N_{ccn} in the cloud layer never exceeds 60 cm^{-3} over the last 3 hours of the simulation; instead, higher values brought in by entrainment and turbulent mixing at the cloud top are continuously mixed throughout the entire boundary layer. Consequently, the CCN concentration is fairly well mixed throughout the boundary layer by the end of simulation (long-dashed line).

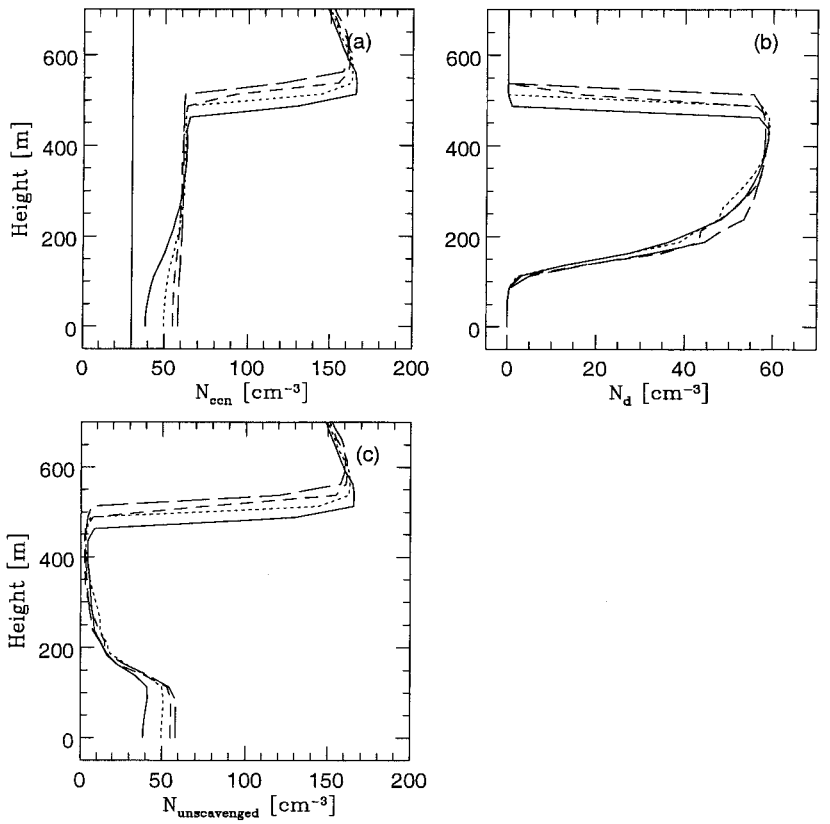

Figure 4. Layer-averaged profiles of (a) potential number of CCN that could be activated N_{ccn}, (b) drop number concentration N_d, and (c) CCN concentrations $N_{unscavenged} = N_{ccn} - N_d$ for N250. Values are layer averages at various times between the second hour and the fifth hour of simulation time in 1 hour increments. The solid line denotes values at 2 hours, the dotted line denotes values at 3 hours, the short-dashed line denotes values at 4 hours, and the long-dashed line denotes values at 5 hours. The solid vertical line at $N_{ccn} = 30$ cm^{-3} denotes the constant value used in the N30 run.

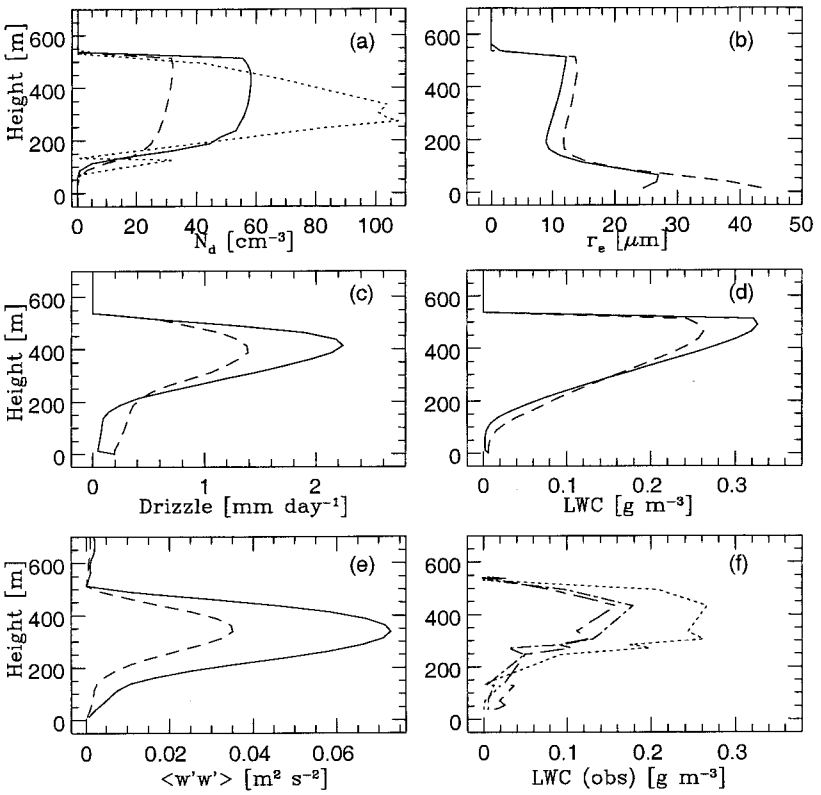

Figure 5. Snapshots of layer-averaged vertical profiles of (a) N_d (the dotted line denotes the measured droplet concentration from the FSSP-100), (b) effective radius r_e, (c) drizzle rate, (d) liquid-water content, (e) vertical velocity variance $\langle w'w' \rangle$ at 5 hours for both N250 and N30, and (f) the observed vertical profiles of LWC from different probes. Line types from Figures 5a to 5e are the same as indicated in Figure 3. (f) Line types are defined as follows: the dotted line denotes the FSSP-100 measurement, the dotted-short-dashed line denotes the Gerber probe measurement, and the short-dashed to long-dashed line denotes the King probe measurement.

Note that the constant value of 30 cm^{-3} used for the N30 run is drawn for reference (solid vertical line). The maximum N_d is of the order of 55–60 cm^{-3}. The near-zero $N_{\text{unscavenged}} = N_{\text{ccn}} - N_d$ (Figure 4c) indicates that almost all of N_{ccn} in the cloud layer are activated to form droplets (N_d), while above and below the cloud layer, $N_{\text{unscavenged}}$ is identical to N_{ccn}. It can be seen that cloud top grows with time (Figure 4), in agreement with Figure 3a.

Snapshots of the layer-averaged N_d, effective radius r_e, drizzle rate, liquid water content LWC, and vertical velocity variance $\langle w'w' \rangle$ at 5 hours for both runs are shown in Figure 5. Also plotted in Figure 5 is the LWC and droplet concentration from different probes used in the observations. The maximum droplet number concentration N_d for N250 is about 60 cm^{-3}, while it is only 30 cm^{-3} for N30 (Figure 5a). Within the cloud region, N_d is approximately constant with height, consistent with observations in the Arctic [e.g., *Curry*, 1986] and in the marine boundary layer [e.g., *Duynkerke et al*., 1995]. The increase in droplet concentration is correlated with the increase in N_{ccn} for N250. As the air containing higher CCN concentration is entrained into the cloudy boundary layer, the CCN are quickly activated to form droplets. Note that the observed N_d in this case varies from 40 to 105 cm^{-3} in the cloud layer. Differences between the modeled and the observations can be attributed to differing sampling and averaging techniques. Also, notice that the measured maximum N_d of 105 cm^{-3}, derived from the FSSP-100 (dotted line), is much higher than the modeled value. This should be borne in mind when comparing other modeled variables with observations.

The layer-averaged effective radius r_e, defined as the ratio between the third and the second moments of the drop distribution (Figure 5b), provides evidence that N250 produces smaller cloud drops than N30. With less drops competing for the available water vapor in the N30 run, drops grow to sizes considerably larger and fall to the subcloud layer, where r_e is significantly higher for N30 than for N250. Note that the values of r_e become progressively less meaningful as the moments tend to zero at heights below 50–100 m.

In the N250 run the drizzle rate (Figure 5c) has a maximum of 2.2 mm d^{-1}, mainly in the cloud layer with almost no drizzle reaching the surface. In the N30 run, however, the maximum is barely two thirds of that of N250 in the cloud layer, but ~16% of the maximum reaches the ground. The lower drizzle rates within the cloud are a result of depletion of cloud water through more drizzle reaching the ground.

The differences between the LWC (Figure 5d) for N30 and N250 are characteristic of the differences between drizzling and nondrizzling clouds [e.g., *Stevens et al*., 1998]. In N250, LWC is about 21% higher in the layer near cloud top and lower near cloud base and in the subcloud layer compared with the N30 run. Drizzle effectively redistributes the liquid water downward with some losses occurring in N30 through sedimentation to the surface. The dynamical response is significant at

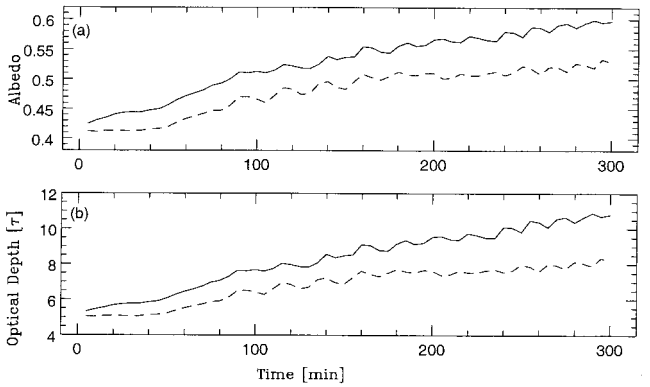

Figure 6. Time evolution of (a) cloud albedo A and (b) cloud optical depth τ with line types as indicated in Figure 3.

this time of the simulation, as expressed by higher $\langle w'w' \rangle$ for the N250 run (Figure 5e).

Figure 5f shows that the maximum observed LWC is in the range from 0.16 g m^{-3} (King and Gerber probe) to 0.26 g m^{-3} (FSSP-100). The modeled LWC averaged over the last 3 hours of simulation (not shown) is of the order of 0.3 g m^{-3}. The higher value of LWC and the lower value of N_d predicted by the model have implications for the cloud radiative response, as shown later.

It is evident in Figure 5 that the increase in CCN concentration through entrainment results in larger N_d, smaller drop sizes, and less drizzle reaching the ground [e.g., *Albrecht*, 1989]. The results shown in Figure 5 are consistent with *Olsson et al.* [1998], who found that higher CCN concentrations produced a cloud with larger cloud top LWC, larger number concentrations, and smaller droplets in their cloud-resolving simulations of warm-season arctic stratus.

The impact of the entrainment of CCN into the cloud on the cloud optical properties is evaluated in Figure 6. Optical depth (in the visible) is defined as

$$\tau \approx \int_{z_b}^{z_t} \int_0^{\infty} 2\pi r^2 n(r, z)\, dr\, dz, \tag{3}$$

where $n(r)$ defines the drop spectrum with respect to radius r, z_b is cloud base, z_t is cloud top, and an asymptotic value of 2 has been assumed for the extinction efficiency [e.g., *Platnick and Twomey*, 1994]. Albedo is calculated using the simple relationship between cloud albedo A and optical depth given by *Bohren* [1987].

$$A \approx \frac{(1-g)\tau}{2 + (1-g)\tau}, \tag{4}$$

where g is the scattering asymmetry factor [*Twomey*, 1991]. At small τ, A is approximately linearly dependent on τ and therefore A is positively correlated with τ. Both A (Figure 6a) and τ (Figure 6b) increase steadily from the beginning of the simulation. According to *Twomey* [1974], τ scales with $N_d^{1/2}$ for clouds of similar r_l. Figure 5a indicates that N_d(N250)/N_d(N30) $\approx$ 60/30 = 2, so their optical depth ratio should scale by $2^{1/3} = 1.26$. Figure 6b indicates that at 200 min, before N30 LWP has begun to lose significant water τ(N250)/τ(N30) $\approx$ 9.5/7.5 = 1.27, so there is excellent agreement with this simple scaling law when the runs have similar LWP. Notice that the differences between the two runs grows larger with time. In the case of N250, A is roughly 7% higher at 120 min and is about 12% higher at 300 min of simulation, while τ is 14% higher at 120 min and 33% higher at 300 min. This is related to the depletion in liquid water in N30 which reduces both τ and A.

Since entrainment is a key element of this study, the entrainment rate w_e (the growth rate of the cloud-top height) is computed as the average $dz_i/dt - w_{\text{sub}}$ over the last 3 hours of the simulation period. Recall that the imposed w_{sub} is about -0.25 cm s^{-1} at the inversion. The estimation of w_e is also provided with observational data based on the jump model [*De Roode and Duynkerke*, 1997], $w_e = -\overline{(w'r_t')_{z_i}}/\Delta r_t$, where Δr_t is the jump of the mean total water across the cloud top, and $\overline{(w'r_t')_{z_i}}$ is the total water entrainment flux right beneath the inversion height. As shown in Table 1, the model results (3 hour average) are slightly larger but compare reasonably well with the observation.

Layer-averaged droplet spectra $n(r)$ are shown in Figure 7 at 5 hours and compared to observed spectra. The observed spectra were measured with a forward scattering spectrometer probe (FSSP-100) and a 1-D optical array probe (260X) mounted on the National Center for Atmospheric Research (NCAR) C-130. The FSSP-100 detects particles with a diameter range of 2–55 μm and has a resolution of about 3 μm. The 260X probe measures particles in the diameter range 12.5–812.5 μm and has a resolution of about 13 μm. Specific calibrations were also made for the instruments used in this experiment. Because the aircraft samples drop spectra along a flight track that is not necessarily representative of the entire cloud we have opted to compare spectra at similar LWC rather than at similar flight altitudes. Figure 7 indicates that broad features of the drop spectra are reasonably well captured by the model; for example, the mode of the spectrum is usually in the correct position. In Figure 7a the modeled mode is at about 3 μm as opposed to 5 μm. The source of the 3 μm mode has been traced to droplet activation occurring just above cloud base. The most notable differences lie in the tendency for the model to overpredict the number concentration of drops in the range 15 μm $< r <$ 80 μm. At the largest drop sizes (100 μm) the 260X tends to show higher concentrations than predicted by the model. This "concavity" in the 260X drop spectra may indicate the presence of ice particles or melted ice particles. Observed spectra often have a significantly stronger mode than the modeled spectra. Examination of the data shows that when

Table 1. Entrainment Rates for Model Runs and Observation

	N30	N250	Obs
dz_i/dt [cm s^{-1}]	0.364	0.388	
w_{sub} [cm s^{-1}]	-0.25	-0.25	
$w_e = dz_i/dt - w_{\text{sub}}$ [cm s^{-1}]	0.614	0.638	
$w_e = -\overline{(w'r_t')_{z_i}}/\Delta r_t$	$\Delta r_t = -0.35$ [g kg^{-1}]	$\overline{(w'r_t')_{z_i}} = 2. \times 10^{-3}$ [g kg^{-1} ms^{-1}]	0.57 [cm s^{-1}]

this occurs, the observed $N_d \approx 100$ cm^{-3} compared to the typical 60 cm^{-3} modeled here. The higher N_d indicate stronger competition for vapor and limited growth so that the differences are consistent with our understanding of droplet growth through condensation and collision-coalescence.

Modeled and observed shortwave downwelling fluxes at the surface (F_s^-) are shown in Figure 8a. F_s^- decreases with time in response to the increase in albedo (cloud shortwave reflectance) and optical depth τ (Figure 6b) for both simulations. Note that F_s^- is systematically lower for the increased CCN (N250) run than for the lower CCN (N30) run. This is consistent with the work of *Curry et al*. [1993], who studied the arctic radiative response to changes in cloud optical properties. They found that increased numbers of CCN cause a larger number of smaller droplets and as drop sizes become smaller, cloud reflectivity increases, reducing the incoming shortwave flux. The observed values of F_s^- are higher than the modeled ones although they do show a similar trend to the modeled values. The decrease in the observed F_s^- with time is mainly due to the increase in solar zenith angle [*Duynkerke and de Roode*, this issue]. Considering the fact that the observed N_d are sometimes as high as 100 cm^{-3} (Figure 5a), one might have expected lower transmission through the observed cloud and therefore an observed F_s^- that is lower than both model results. However, an integration of the observed LWC profiles (Figure 5f) yields a LWP somewhat less than the modeled one and since to first order $\tau \approx 1.5$ LWP/r_e the lower LWP reduces τ and A and increases F_s^-. (A reduction in r_e due to the larger N_d is not sufficient to offset this.) Longwave downwelling fluxes at the surface (not shown) are identical between both runs and the observed value of $\approx$280 W m^{-2}.

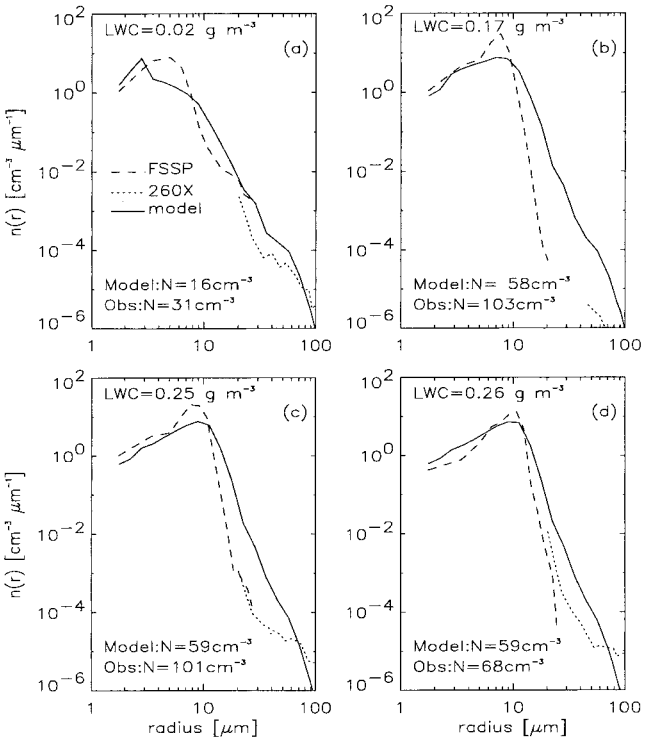

Figure 7. Layer-averaged droplet spectra for the N250 run compared with observed droplet spectra $n(r)$ [cm^{-3} μm^{-1}] derived from both the FSSP-100 and the 260X probes at different LWC values as labeled on the plots.

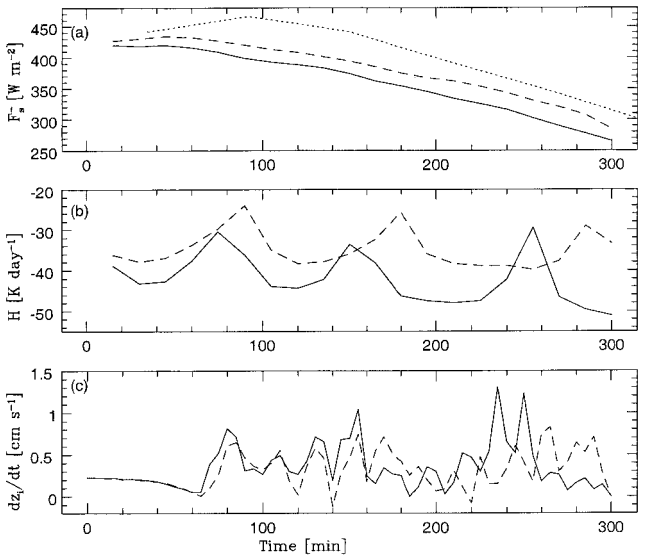

Figure 8. Temporal evolution of (a) downwelling shortwave fluxes at the surface, (b) cloud-top radiative cooling, and (c) growth rate of the cloud top = dz_i/dt for both runs with line types as indicated in Figure 3 except that the dotted line denotes the observed flux in Figure 8a.

The total cloud-top radiative cooling exhibits an irregular periodic variation for both runs (Figure 8b), but differences are clearly present. A number of features are noteworthy. The maximum cooling is about -50 K d^{-1} for the N250 run and about -30 K d^{-1} for the N30 run. The reduction in the rate of radiative cooling for the N30 run is due to the reduction in liquid-water content near cloud top by drizzle sedimentation [e.g., *Chen and Cotton*, 1987]. From Figures 8b and 8c, it can be seen that the maximum entrainment is correlated with reduced cooling rates. The correlation between the entrainment and the cloud-top cooling may be attributed to the following: cloud-top cooling promotes turbulence and entrainment and when the entrainment is vigorous, the enhanced mixing of warmer and drier air from above leads to a reduction in the cloud-top cooling. Note that the periodicity (Figure 8b) grows longer with time in N30. The coupling among drizzle, radiative, and turbulence modulates the entrainment process. Each of these processes are associated with their own response timescales. For an optically thick cloud (the N250 run), a higher value of liquid-water path promotes a faster recovery of the radiative cooling reduced by drizzle and therefore a shorter time scale in the cycle.

5. Discussion

An interesting result emerging from the N250 run is that the rate of change of the CCN concentration in the cloud layer, and its influence on the cloud, is tied to the change in inversion layer height z_i. As the inversion height rises, one would expect the concentration of CCN in the boundary layer to increase with time until it reaches values greater than 150 cm^{-3} as the boundary layer is progressively contaminated by the dirtier air from above. In the current simulations we have shown that the maximum concentration of CCN in the cloud layer never exceeds 60 cm^{-3}. Simple calculations given below provide an explanation for this (B. Stevens, personal communication, 1999). By mass continuity the only way for the inversion to rise

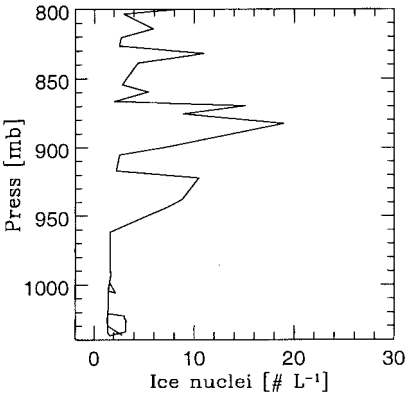

Figure 9. Vertical profile of ice-forming nuclei measured with the Colorado State University CFD ice nucleus counter. Courtesy of D. Rogers of CSU. Note that the pressure level at 960 mbar is equivalent to the modeled inversion height (530 m).

is if fluid from above the inversion is mixed into the boundary layer. Quantitatively, we initially have $N_{\text{ccn}} = 30\ \text{cm}^{-3}$ in the cloud layer and $N_{\text{ccn}} = 250\ \text{cm}^{-3}$ above the inversion height (Figure 1), while z_i rises from 460 to 530 m by the end of the simulation (Figure 3a). The maximum change in the CCN concentration in the cloud layer due to entrainment for the 5 hour long simulation will be approximately

$$N_f = (N_0 \times z_{i0} + N_i \times (z_{if} - z_{i0}))/z_{if} = N_i - \frac{z_{i0}}{z_{if}}(N_i - N_0), \tag{5}$$

where z_{i0} and z_{if} denote initial and final values of z_i, respectively; N_0 and N_i represent the initial values of N_{ccn} in the cloud and above inversion, and N_f represents the predicted value of N_{ccn}. By substituting the values produced in this study, we have $N_f = 250 - 460/530\ (250 - 30) = 59\ \text{cm}^{-3}$, which is in agreement with the number we have simulated in the high CCN case.

The simple calculation given above suggests that the effect of polluted layers aloft on underlying clouds will depend, at least in part, on the rate of increase in z_i. It is probable that the impact of the entrained CCN on the simulated cloud would be greater if z_i rises faster than it does in this study, provided that there are no significant changes in LWP. This result suggests that we may be able to predict changes in cloud optical properties either due to the contamination of clouds, as in this study, or due to dilution in cases where cleaner air overlies dirtier air as seen in the ASTEX Lagrangian II experiment [*Bretherton et al*., 1995]. By combining the expression relating N_d to boundary layer evolution (equation (5)) with *Twomey*'s [1974] $\tau \approx N_d^{1/3}$ scaling law and *Bohren*'s [1987] simple relationship between cloud albedo A and optical depth (see (4) in section 3 for detail), we can predict cloud albedo changes in response to changes in N_{ccn} for a given LWC, or LWP.

Using $\tau_0 \approx N_0^{1/3}$ to represent for the constant CCN case and $\tau_f \approx N_f^{1/3}$ for the high CCN at the inversion case, we have, at constant LWP,

$$\frac{\tau_f}{\tau_0} = \left(\frac{N_f}{N_0}\right)^{1/3}. \tag{6}$$

From the two simulations we have $N_0 = 30\ \text{cm}^{-3}$, $N_f = 60\ \text{cm}^{-3}$, $\tau_0 = 7.5$ at 200 min (see Figure 6b), and $\tau_f = 7.5 \times (60/30)^{1/3} = 9.4$, which is very close to the number 9.5 calculated directly from the model. Similarly, we can derive the A_f from (4) and (5) as

$$\frac{A_f}{A_0} \approx \frac{\tau_f}{\tau_0}\frac{2 + (1-g)\tau_0}{2 + (1-g)\tau_f} \tag{7}$$

by substituting $\tau_0 = 7.5$, $\tau_f = 9.4$ (from (6)), $A_0 = 0.51$, we have $A_f = 0.58$, which agrees very well with the number directly from the model.

Combining (5) and (6), we have a general expression predicting the change in cloud optical depth as a function of the change in z_i and the N_{ccn} differential across the boundary layer:

$$\frac{\tau_f}{\tau_0} = \left[\frac{N_i}{N_0}\left(1 - \frac{z_{i0}}{z_{if}}\right) + \frac{z_{i0}}{z_{if}}\right]^{1/3}. \tag{8}$$

It should be stressed that the above derivation proceeds under the premise that LWC or LWP remains close to constant and that neither entrainment, nor drizzle change the LWP significantly. In general, the extent to which this holds true will depend on the thermodynamic properties and aerosol characteristics of the air overlying the boundary layer.

This study indicates that the estimation of z_i is central to boundary layer studies with implications for cloud dynamics, microphysics, and cloud optical properties:

1. A boundary layer that rises rapidly and entrains warm, dry air will tend to produce a thinner, higher cloud with lower LWP. Entrainment of warm, dry free tropospheric air will also result in poor vertical mixing if the boundary layer gets too deep. It has been shown by many others that the same entrained air, under certain condition, can descend unstably, enhance TKE at cloud top, and promote more entrainment. Eventually, this feedback mechanism (commonly referred to as cloud-top entrainment instability) can cause the dissipation of the cloud [e.g., *Lilly*, 1968; *Randall*, 1980; *Deardorff*, 1980; *MacVean and Mason*, 1990; *Duynkerke*, 1993; *De Roode and Duynkerke*, 1997]. Shallow boundary layers that do not rise may produce significant drizzle, which also reduces LWP. In some instances a boundary layer that deepens slowly may dry sufficiently such that drizzle is suppressed and LWP is maintained approximately constant [*Stevens*, 1996].

2. The rate at which free tropospheric aerosol particles (some subset of which are CCN) are entrained into the cloud layer will directly affect cloud optical depth and albedo, and indirectly affect boundary layer dynamics by modifying cloud-top cooling rates [e.g., *Olsson et al*., 1998] and modifying drizzle. The effect of drizzle on boundary layer dynamics has been considered in depth by *Stevens et al*. [1998].

3. A small fraction of the aerosol population (concentrations of the order of a few per liter to a few tens per liter) may act as ice-forming nuclei (IFN). At high latitudes the entrainment of free tropospheric air into stratiform clouds experiencing subzero temperatures could be strongly impacted by these IFN [*Harrington et al*., 1999; *Jiang et al*., 2000].

Note that the observed IFN sounding for this case exhibited a sharp increase in IFN concentrations above the inversion (Figure 9, courtesy of D. Rogers). Thus had this case been cold enough for vigorous participation of the ice phase, we speculate that perturbation of the thermodynamic, dynamic, and radiative properties of the arctic boundary layer by entrainment would have been much greater.

6. Summary

Results from two large eddy simulations of the May 18, 1998, SHEBA/FIRE case have been presented. One simulation uses the thermodynamic and CCN sounding data taken from the SHEBA/FIRE research flight RF05 (May 18, 1998). The other uses a CCN profile of smaller constant value.

The major results of the present study may be summarized as follows: The simulation with the observed CCN profile (high CCN) shows that the increase in CCN concentration resulting from entrainment results in a higher droplet concentration, smaller drop sizes, more liquid water retained in the cloud layer, and less drizzle reaching the surface. The smaller drops also cause a decrease in the surface shortwave flux.

Although the cloud optical properties respond to the change in CCN concentration from the beginning of the simulations with higher values of cloud albedo A and cloud optical depth τ, liquid water path does not show significant variations until 4 hours into the simulations.

The differences between the high CCN run and the low CCN run show characteristics of the differences between drizzling and nondrizzling clouds [e.g., *Steven et al*., 1998], namely, that drizzle redistributes heat and vapor in the vertical in a manner that stabilizes the boundary layer. In the case under consideration the dynamic response becomes significant at the end of the 5 hour simulation in the high CCN run, as reflected in more vigorous eddies. To quantify whether the entrained CCN in N250 systematically leads to a greater dynamic response requires simulations beyond the 5 hours.

Higher entrainment rates are associated with stronger cloud-top cooling. This is consistent with the study of *Deardorff* [1981], who showed that large values of cloud-top cooling are more favorable for entrainment and the production of mixed-layer convection.

We have shown that the contamination of the cloud is much less than the large jump in CCN at the inversion might imply because the contamination of the cloud by the polluted air aloft is limited by the rate at which the boundary layer top z_i rises. In spite of the more modest contamination there are still noticeable differences in cloud optical properties, and suppression of drizzle makes these differences even stronger.

This work underscores the fact that knowledge of boundary layer deepening is critical to prediction of cloud optical properties. This is true both from the thermodynamic point of view where the properties of the entrained air affect bulk cloud features such as LWP as well as from the microscale point of view where aerosol gradients across the top of the boundary layer can alter microphysical processes and, in turn, cloud optical properties. This issue is even more critical for mixed phase clouds given the sensitivity of such clouds to even small concentrations (order of 1 L^{-1}) of ice-forming nuclei [*Jiang et al*., 2000].

Acknowledgments. B. Stevens is thanked for useful discussions. D. Baumgardner and K. Laursen are thanked for providing the initial sounding information. D. Rogers is thanked for providing the Ice Nuclei data used in creating Figure 9. The comments of two anonymous reviewers greatly improved the clarity of this manuscript. This research was supported by grants from the NASA/FIRE III (NAG-1-2045). G. Feingold was partially supported by a NOAA Office of Global Programs grant. P.G. Duynkerke was supported for the participation in the SHEBA experiment by the Netherlands Geosciences Foundation (GOA) with financial aid (grant 750.295.03) from the Netherlands Organization for Scientific Research (NWO). The last author thanks NCAR and its sponsor, the National Science Foundation, for allowing him to use the C130 observational data. Finally the IMAU wishes to thank the many people of the FIRE/SHEBA community for giving logistical support by bringing the equipment to the SHEBA ice camp and for assisting on the site.

References

Albrecht, B. A., Aerosols, cloud microphysics, and fractional cloudiness, *Science*, *245*, 1227–1230, 1989.

Baker, M. B., R. G. Gorbin, and J. Latham, The influence of entrainment on the evolution of cloud droplet spectra, I, A model of inhomogeneous mixing, *Q. J. R. Meteorol. Soc*., *106*, 581–598, 1980.

Barrie, L. A., Arctic air pollution: An overview of current knowledge, *Atmos. Environ*., *19*, 1995–2010, 1986.

Bohren, C. F., Multiple scattering of light and some of its observable consequences, *Am. J. Phys*., *55*, 524–533, 1987.

Bretherton, C. S., P. Austin, and S. T. Siems, Cloudiness and marine boundary layer dynamics in the ASTEX Lagrangian experiments, part II, Cloudiness, drizzle, surface fluxes, and entrainment, *J. Atmos. Sci*., *52*, 2724–2735, 1995.

Chen, C., and W. R. Cotton, The physics of the marine stratocumulus-capped mixed layer, *J. Atmos. Sci*., *44*, 2951–2977, 1987.

Clarke, A. D., Atmospheric nuclei in the remote midtroposphere: Their nature, concentration, and evolution, *J. Geophys. Res*., *98*, 20,633–20,647, 1993.

Clarke, A. D., T. Uehara, and J. N. Porter, Lagrangian evolution of an aerosol column during the Atlantic Stratocumulus Transition Experiment, *J. Geophys. Res*., *101*, 4351–4362, 1996.

Clarke, A. D., T. Uehara, and J. N. Porter, Atmospheric nuclei and related aerosol fields over the Atlantic: Clean subsiding air and continental pollution during ASTEX, *J. Geophys. Res*., *102*, 25,281–25,292, 1997.

Considine, G., and J. A. Curry, Effects of entrainment and droplet sedimentation on the microphysical structure of stratus and stratocumulus clouds, *Q. J. R. Meteorol. Soc*., *124*, 123–150, 1998.

Curry, J. A., Interactions among turbulence, radiation, and microphysics in Arctic stratus clouds, *J. Atmos. Sci*., *43*, 90–106, 1986.

Curry, J. A., Interactions among aerosols, clouds and climate of the Arctic Ocean, *Sci. Total Environ*., *160/161*, 777–791, 1995.

Curry, J. A., E. E. Ebert, and J. Schramm, Impact of clouds on surface radiation balance of the Arctic Ocean, *Meteorol. Atmos. Phys*., *57*, 197–217, 1993.

Deardorff, J. W., Cloud-top entrainment instability, *J. Atmos. Sci*., *37*, 131–147, 1980.

Deardorff, J. W., On the distribution of mean radiative cooling at the top of a stratocumulus-capped mixed layer, *Q. J. R. Meteorol. Soc*., *107*, 191–202, 1981.

De Roode, S. R., and P. G. Duynkerke, Observed Lagrangian transition of stratocumulus into cumulus during ASTEX: Mean state and turbulence structure, *J. Atmos. Sci*., *54*, 2157–2173, 1997.

Duda, D. P., G. L. Stephens, B. Stevens, and W. R. Cotton, Effects of aerosol and horizontal inhomogeneity on the broadband albedo of marine stratus: Numerical simulations, *J. Atmos. Sci*., *53*, 3757–3769, 1996.

Duynkerke, P. G., The stability of cloud top with regard to entrainment: Amendment of theory of cloud-top entrainment instability, *J. Atmos. Sci*., *50*, 495–502, 1993.

Duynkerke, P. G., H. Q. Zhang, and P. J. Jonker, Microphysical and turbulent structure of nocturnal stratocumulus as observed during ASTEX, *J. Atmos. Sci*., *52*, 2778–2787, 1995.

Duynkerke, P. G., and S. R. de Roode, Surface energy balance and turbulence characteristics observed at the SHEBA ice camp during FIRE III, *J. Geophys. Res*., this issue.

Feingold, G., B. Stevens, W. R. Cotton, and R. L. Walko, An explicit cloud microphysical/LES model designed to simulate the Twomey effect, *Atmos. Res*., *33*, 207–233, 1994.

Feingold, G., B. Stevens, W. R. Cotton, and A. S. Frisch, On the relationship between drop in-cloud residence time and drizzle production in stratocumulus clouds, *J. Atmos. Sci*., *53*, 1108–1122, 1996a.

Feingold, G., S. M. Kreidenweis, B. Stevens, and W. R. Cotton, Numerical simulation of stratocumulus processing of cloud condensation nuclei through collision-coalescence, *J. Geophys. Res*., *101*, 21,391–21,402, 1996b.

Feingold, G., R. Boers, B. Stevens, and W. R. Cotton, A modeling study of the effect of drizzle on cloud optical depth and susceptibility, *J. Geophys. Res*., *102*, 13,527–13,534, 1997.

Feingold, G., W. R. Cotton, S. M. Kreidenweis, and J. T. Davis, Impact of giant cloud condensation nuclei on drizzle formation in marine stratocumulus: Implications for cloud radiative properties, *J. Atmos. Sci*., *56*, 4100–4117, 1999.

Harrington, J. Y., T. Reisin, W. R. Cotton, and S. M. Kreidenweis, Cloud resolving simulations of arctic stratus, part II, Transition-season clouds, *Atmos. Res*., *51*, 45–75, 1999.

Harrington, J. Y., G. Feingold, and W. R. Cotton, Radiative impacts on the growth of a population of drops within simulated summertime arctic stratus, *J. Atmos. Sci*., *57*, 766–785, 2000.

Hudson, J. G., An instantaneous CCN spectrometer, *J. Atmos. Oceanic Technol*., *6*, 1055–1065, 1989.

Jiang, H., W. R. Cotton, J. O. Pinto, J. A. Curry, and M. J. Weissbluth, Cloud resolving simulations of mixed-phase arctic stratus observed during BASE: Sensitivity to concentration of ice crystals and large-scale heat and moisture advection, *J. Atmos. Sci*., *57*, 2105–2117, 2000.

Lilly, D. K., Models of cloud-topped mixed layers under a strong inversion, *Q. J. R. Meteorol. Soc*., *94*, 292–309, 1968.

Louis, J. F., A parameteric model of vertical eddy fluxes in the atmosphere, *Boundary Layer Meteorol*., *17*, 187–202, 1979.

MacVean, M. K., and P. J. Mason, Cloud-top entrainment instability through small-scale mixing and its parameterization in numerical models, *J. Atmos. Sci*., *47*, 1012–1030, 1990.

Mitchell, D. L., A. Macke, and Y. Liu, Modeling cirrus clouds, part II, Treatment of radiative properties, *J. Atmos. Sci*., *53*, 2967–2988, 1996.

Olsson, P. Q., J. Y. Harrington, G. Feingold, W. R. Cotton, and S. M. Kreidenweis, Exploratory cloud-resolving simulations of boundary-layer Arctic stratus clouds, part I, Warm-season clouds, *Atmos. Res*., *47-48*, 573–597, 1998.

Platnick, S., and S. Twomey, Determining the susceptibility of cloud albedo to changes in droplet concentration with the advanced very high resolution radiometer, *J. Appl. Meteorol*., *33*, 334–347, 1994.

Raes, F., Entrainment of free tropospheric aerosols as a regulating mechanism for cloud condensation nuclei in the remote marine boundary layer, *J. Geophys. Res*., *100*, 2893–2903, 1995.

Randall, D. A., Conditional instability of the first kind upside down, *J. Atmos. Sci*., *37*, 125–130, 1980.

Ritter, B., and J-F. Geleyn, A comprehensive radiation scheme for numerical weather prediction models with potential applications in climate simulations, *Mon. Weather Rev*., *120*, 303–325, 1992.

Stevens, B., On the dynamics of precipitating stratocumulus, thesis, 140 pp., Colorado State Univ., Fort Collins, Colo., 1996.

Stevens, B., G. Feingold, W. R. Cotton, and R. L. Walko, Elements of the microphysical structure of numerically simulated nonprecipitating stratocumulus, *J. Atmos. Sci*., *53*, 980–1006, 1996.

Stevens, B., W. R. Cotton, G. Feingold, and C-H Moeng, Large-eddy simulations of strongly precipitating, shallow, stratocumulus-topped boundary layers, *J. Atmos. Sci*., *55*, 3616–3638, 1998.

Su, C.-W., S. K. Krueger, P. A. McMurty, and P. H. Austin, Linear eddy modeling of droplet spectral evolution during entrainment and mixing in cumulus clouds, *Atmos. Res*., *47-48*, 41–58, 1998.

Telford, J. W., and S. T. Chai, A new aspect of condensation theory, *Pure Appl. Geophys*., *118*, 720–742, 1980.

Telford, J. W., and P. B. Wagner, Observations of condensation growth determined by entity type mixing, *Pure Appl. Geophys*., *119*, 934–965, 1981.

Tripoli, G. J., and W. R. Cotton, The use of ice-liquid water potential temperature as a thermodynamic variable in deep atmospheric models, *Mon. Weather Rev*., *109*, 1094–1102, 1981.

Tzivion, S., G. Feingold, and Z. Levin, An efficient numerical solution to the stochastic collection equation, *J. Atmos. Sci*., *44*, 3139–3149, 1987.

Tzivion, S., G. Feingold, and Z. Levin, The evolution of raindrop spectra, part II, Collisional collection/breakup and evaporation in a rain shaft, *J. Atmos. Sci*., *46*, 3312–3327, 1989.

Twomey, S., Pollution and planetary albedo, *Atmos. Environ*., *8*, 1251–1265, 1974.

Twomey, S., Aerosols, clouds and radiation, *Atmos. Environ*., *Part A*, *25*, 2435–2442, 1991.

W. R. Cotton and H. Jiang, Department of Atmospheric Science, Colorado State University, Fort Collins, CO 80523. (cotton@atmos.colostate.edu; jiang@atmos.colostate.edu)

G. Feingold, NOAA, Environmental Technology Laboratory, 325 Broadway, Boulder, CO 80303. (gfeingold@etl.noaa.gov)

P. G. Duynkerke, Institute for Marine and Atmospheric Research Utrecht (IMAU), Utrecht University, Utrecht, The Netherlands. (P.G.Duynkerke@phys.uu.nl)

(Received December 22, 1999; revised April 24, 2000;
accepted May 5, 2000.)